Nonlinear Spacecraft Dynamics with a Flexible Appendage, Damping, and Moving Internal Submasses

Andrew J. Miller* and Gary L. Gray†
Pennsylvania State University, University Park, Pennsylvania 16802
and
Andre P. Mazzoleni‡
Texas Christian University, Fort Worth, Texas 76129

We study the attitude dynamics of a single-body spacecraft that is perturbed by the motion of small oscillating submasses, a small flexible appendage constrained to undergo only torsional vibration, and a rotor immersed in a viscous fluid. We are interested in the chaotic dynamics that can occur for certain sets of the physical parameter values of the spacecraft when energy dissipation acts to drive the body from minor to major axis spin. Energy dissipation, which is present in all spacecraft systems and is the mechanism that drives the minor to major axis transition, is implemented via the rotor. We not only obtain an analytical test for chaos in terms of satellite parameters using Melnikov's method, but we also use extensive numerical simulation to check the range of validity of the Melnikov result.

Introduction

THE determination and control of attitude evolution are important problems in modern spacecraft dynamics. For example, a single-body spacecraft is directionally unstable in the presence of energy dissipation when perturbed from spinning about its minor axis.[1] In the absence of active stabilization, the body will eventually reorient itself and spin about its major axis. In addition, the presence of oscillating subbodies or other perturbations can produce chaos and its inherent unpredictability in some or all of the phase space traversed by the spacecraft during this or any other attitude maneuver. Because it is often important to be able to predict accurately the timing or sequence of attitude maneuvers and because the presence of chaotic dynamics could render useless any attempt at this prediction, it is important to be able to understand when chaos will play a role in the attitude dynamics of a spacecraft.

The equations of motion describing the attitude dynamics of complex nonrigid spacecraft are readily derived, but their analytical solution is elusive. In fact, if the system is nonlinear and, thus, potentially chaotic, these solutions are fundamentally unobtainable. On the other hand, solutions to these highly nonlinear equations can be obtained for specific parameter values using numerical simulation, but many interesting features of the dynamics can be lost in the numerical data. Fortunately, a great deal of physical insight into the behavior of these complex systems can be obtained by using a simpler rigid body with perturbations approximation for modeling and analyzing the spacecraft. This paper deals with the dynamics of the attitude transition from minor axis to major axis spin of a rigid body that is being perturbed by small oscillating submasses and a flexible appendage. In addition, energy dissipation is implemented via a rotor immersed in a viscous fluid. In particular, we are interested in the occurrence of chaotic dynamics during spin-axis transition.

Some aspects of related attitude maneuvers have been studied for dual-spin spacecraft. These spacecraft are reoriented by spin up or spin down of rotors relative to the main spacecraft body. Attitude resonances in these maneuvers, occurring during spin up or spin down, have been investigated using perturbation techniques and numerical simulation (for example, see Refs. 2–9). In addition, Or[10] has studied chaotic dynamics of a symmetric dual-spin spacecraft subjected to internally oscillating torque and coulomb friction using Melnikov's method (see Refs. 11–13). Or computes bifurcation diagrams and compares his analytical results with numerical simulations.

In the case of single-body satellites, the direction and control of the final major axis orientation have been studied,[14−19] as have the dynamics and evolution of the maneuver itself, as found in work by Tsiotras and Longuski[20] and Longuski and Tsiotras,[21,22] in which they study the attitude evolution of near-symmetric rigid bodies under a variety of torque conditions. Other work has been done with perturbation studies of spacecraft with elastic and/or dissipative elements by Chernous'ko[23,24] and the analytical and numerical study by Kaplan and Cenker[17] and Kaplan and Beck[25] of the use of the apogee motor with paired satellites technique to deploy pairs of satellites into high circular orbits. Excellent reviews of some of this work and much more may be found in Refs. 26 and 27.

Some other closely related work examines chaos in spacecraft attitude dynamics when the perturbations are Hamiltonian (for example, see Refs. 28–30). In other recent work, Tong and Tabarrok[31] use Melnikov's method to investigate the attitude motion of self-excited rigid bodies subject to small perturbation torques in a viscous medium. Cooper and Bishop[32] use Melnikov's method to study chaotic attitude dynamics of a rigid body driven by sinusoidally varying torques. Meehan and Asokanthan[33,34] study chaotic motion in a rotating body subjected to sinusoidally varying external torques and containing a circumferential nutation damper. They use time histories, phase space analyses, Poincaré maps, Lyapunov exponents, and bifurcation diagrams to study the onset of chaos for a range of forcing amplitudes and frequencies and to understand the effect of control strategies on these chaotic systems.

This present work is an extension of earlier work done by Gray et al.[35−38] and Miller and Gray[39] in which they analytically investigated chaotic attitude dynamics occurring in simple spacecraft systems. The present work differs from Refs. 35–39 in that we are not only able to obtain an analytical criterion for the prediction of chaotic dynamics, but we are able to compare the results of the analysis with numerical simulations to gain an understanding of the range of validity of the analysis. In addition, we are able to obtain some insight into which of the parameters of the system most profoundly influence the onset of chaotic dynamics or period-n limit cycles. In fact, we are able to show that in most parameter regions, the analytical predictor for chaotic dynamics also does very well at predicting the onset of limit cycles.

*Graduate Assistant, 212 Earth and Engineering Sciences Building, Department of Engineering Science and Mechanics.
†Associate Professor, 212 Earth and Engineering Sciences Building, Department of Engineering Science and Mechanics; gray@engr.psu.edu.
‡Associate Professor, Department of Engineering; a.mazzoleni@tcu.edu.

Model Description

The spacecraft model considered (Fig. 1a) is a system composed of a rigid carrier body b, with an elastic appendage a, a pair of oscillating subbodies m, and a rotor $\mathcal{R}$ immersed in a viscous fluid $\mathcal{F}$. This model is assumed to be free of any external moments such as gravity-gradient effects or atmospheric drag. The center of mass for the entire system, including carrier body b, appendage a, subbodies m, and rotor $\mathcal{R}$ is located at $\mathcal{CM}$. An orthogonal coordinate frame, e_1, e_2, and e_3, is attached to the carrier body and originates from the system's center of mass $\mathcal{CM}$. The oscillating subbodies m are displaced from their rest position along the e_1 axis by a prescribed periodic function of time $\eta(t)$. When $\eta(t) = 0$, the position of the subbodies is the distance ℓ from $\mathcal{CM}$. Because the subbodies are always positioned symmetrically on each side of the system's center of mass, their motion does not change the location of the system's mass center. The mass moment of inertia matrix of the subbodies with respect to the carrier body coordinate frame is diag$\{0, \Delta + 2m\ell^2, \Delta + 2m\ell^2\}$, where $\Delta \triangleq \Delta(t) = 2m\eta(t)[\eta(t) + 2\ell]$ will represent the time-dependent terms in the equations of motion. The mass moment of inertia matrix of the carrier body b is given to be diag$\{I_{b1}, I_{b2}, I_{b3}\}$, and the inertia matrix of the carrier body and subbodies together becomes diag$\{I_{b1}, I_{b2} + \Delta + 2m\ell^2, I_{b3} + \Delta + 2m\ell^2\}$.

Appendage a is modeled by a rigid-tip mass m_a joined to the carrier body b by an elastic rod of length L and of negligible mass. The center of mass of appendage a is located at $\mathcal{CM}_a$, a distance d along the e_1 axis. A second orthogonal coordinate frame, ζ_1, ζ_2, and ζ_3, is attached to the appendage at $\mathcal{CM}_a$ such that the e_1 and ζ_1 axes are collinear. For the appendage, the mass moment of inertia matrix with respect to the appendage coordinate frame ζ_1, ζ_2, and ζ_3, is diag$\{A_a, B_a, C_a\}$.

Rotor $\mathcal{R}$ spins about the e_2 axis and is immersed in a fluid $\mathcal{F}$ with coefficient of viscous damping γ. We define the inertia matrix for the rotor as diag$\{I_{r1}, I_{r2}, I_{r1}\}$ with respect to the e_1, e_2, and e_3 frame.

Next, quantities describing the motion of the model will be introduced. The inertial angular velocity vector $\boldsymbol{\omega}$ of the carrier body b in the body-fixed reference frame is defined to be $\boldsymbol{\omega} = \omega_1 \hat{e}_1 + \omega_2 \hat{e}_2 + \omega_3 \hat{e}_3$, where $\hat{e}_1, \hat{e}_2$, and $\hat{e}_3$ represent an orthonormal basis corresponding to the e_1, e_2, and e_3 coordinate frame. The motion of the tip mass on the appendage is limited to rotation about the e_1 axis (cf. Fig. 1b) and is defined by the angle of twist α. No flexural bending or warping of the connecting rod is permitted. This

type of motion is possible if, for example, the appendage is constrained by a system of guy wires.[40,41] As a result, motion of the appendage does not shift the center of mass of the system, $\mathcal{CM}$. The connecting rod has a circular cross section and a torsional stiffness $K = JG/L$, where J is the polar area moment of inertia, G is the shear modulus, and L is the length of the rod. The appendage can rotate at rate $\dot{\alpha}$ relative to the carrier body. The rotor spins about the e_2 axis at a rate of ω_r relative to the carrier body.

Equations of Motion

Derivation of the Equations of Motion

We will use Lagrangian mechanics to derive all of the equations of motion. Note that with this approach the angular velocity components ω_1, ω_2, and ω_3 are not derivatives of corresponding generalized position variables. The velocity components ω_1, ω_2, and ω_3 are considered to be derivatives of quasi coordinates and a special formulation Lagrange's equations for quasi coordinates must be used.[42]

The kinetic energy of the carrier body and the subbodies is given by

$$T_b = \tfrac{1}{2}\left[I_{b1}\omega_1^2 + \left(I_{b2} + \Delta + 2m\ell^2\right)\omega_2^2 + \left(I_{b3} + \Delta + 2m\ell^2\right)\omega_3^2\right] \quad (1)$$

We transform the inertia matrix of appendage so that its components are expressed in the body-fixed e_1, e_2, and e_3 frame instead of the appendage-fixed ζ_1, ζ_2, and ζ_3 frame, and the kinetic energy of the appendage is now derived to be

$$T_a = \tfrac{1}{2}\left[A_a(\omega_1 + \dot{\alpha})^2 + B_a(\omega_2 \cos\alpha + \omega_3 \sin\alpha)^2 \right.$$
$$\left. + C_a(\omega_3 \cos\alpha - \omega_2 \sin\alpha)^2 + m_a d^2\left(\omega_2^2 + \omega_3^2\right)\right] \quad (2)$$

Finally, the kinetic energy of the rotor is derived as

$$T_{\mathcal{R}} = \tfrac{1}{2}\left[I_{r1}\omega_1^2 + I_{r2}(\omega_2 + \omega_r)^2 + I_{r1}\omega_3^2\right] \quad (3)$$

The only component of the spacecraft that contributes to the potential energy is the torsional rod joining the carrier body to the tip mass of the appendage. This rod has torsional stiffness K, and thus, its potential energy is given by

$$V = \tfrac{1}{2}K\alpha^2 \quad (4)$$

where, again, α is the angle of twist of the rod. The Lagrangian $\mathcal{L}$ is found by summing the kinetic energies given in Eqs. (1–3) and subtracting the potential energy in Eq. (4). This gives the Lagrangian of the entire spacecraft as

$$\mathcal{L} = \tfrac{1}{2}\left[A_b\omega_1^2 + (B_b + \Delta)\omega_2^2 + (C_b + \Delta)\omega_3^2 + I_r\omega_r(2\omega_2 + \omega_r)\right.$$
$$- K\alpha^2 + A_a(\omega_1 + \dot{\alpha})^2 + B_a(\omega_2 \cos\alpha + \omega_3 \sin\alpha)^2$$
$$\left. + C_a(\omega_3 \cos\alpha - \omega_2 \sin\alpha)^2 + m_a d^2\left(\omega_2^2 + \omega_3^2\right)\right] \quad (5)$$

where we define $A_b \triangleq I_{b1} + I_{r1}$, $B_b \triangleq I_{b2} + 2m\ell^2 + I_{r2}$, $C_b \triangleq I_{b3} + 2m\ell^2 + I_{r1}$, and $I_r \triangleq I_{r2}$. We make these substitutions to combine spacecraft parameters that do not vary with time. The quantities A_b, B_b, and C_b represent the principle mass moments of inertia of the carrier body added to the mass moments of inertia of the subbodies and rotor at rest relative to the carrier body. In addition, we will assume that $A_b < B_b < C_b$ to simplify the analysis. The assumption of unequal principal mass moments of inertia is necessary for the application of Melnikov's method.

We now apply Lagrange's equations for quasi coordinates to Eq. (5) to obtain three of the five equations of motion. Lagrange's equation of motion for these particular quasi coordinates is given by Meirovitch,[42] to be

$$\frac{\mathrm{d}}{\mathrm{d}t}\left\{\frac{\partial\mathcal{L}}{\partial\boldsymbol{\omega}}\right\} + \begin{bmatrix} 0 & -\omega_3 & \omega_2 \\ \omega_3 & 0 & -\omega_1 \\ -\omega_2 & \omega_1 & 0 \end{bmatrix}\left\{\frac{\partial\mathcal{L}}{\partial\boldsymbol{\omega}}\right\} = \{\mathcal{N}\} \quad (6)$$

where $\{\partial\mathcal{L}/\partial\boldsymbol{\omega}\}$ is the gradient vector of the Lagrangian with respect to the angular velocity $\boldsymbol{\omega}$ and $\{\mathcal{N}\}$ is a vector of torque components, which are all assumed to be zero.
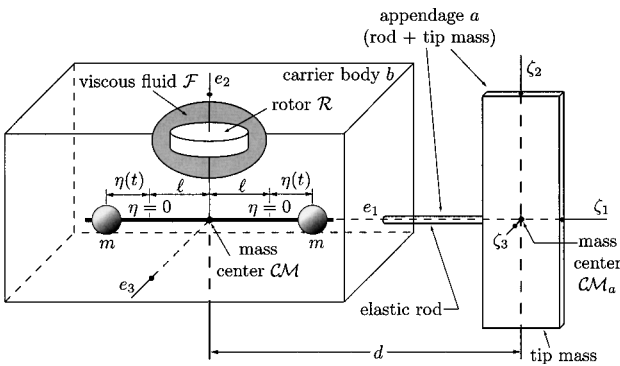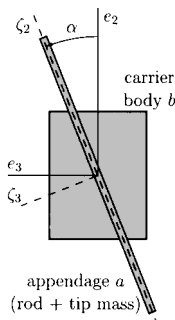

Fig. 1a   Spacecraft model.

Fig. 1b   Profile view of spacecraft in a deformed state.

Evaluating Eq. (6) will give us three equations of motion in terms of the angular velocity components and their time derivatives. Instead, we would like to write the equations in terms of components of the body angular momentum vector $\boldsymbol{h} = h_1\hat{e}_1 + h_2\hat{e}_2 + h_3\hat{e}_3$ because the phase space of the differential equations in terms of the angular momentum components is spherical rather than ellipsoidal as it is in body angular velocity components. Since $\boldsymbol{h} = \{\partial\mathcal{L}/\partial\boldsymbol{\omega}\}$ (see Ref. 43), Eq. (6) becomes

$$\frac{\mathrm{d}\boldsymbol{h}}{\mathrm{d}t} + \boldsymbol{\omega} \times \boldsymbol{h} = \{\mathcal{N}\} = 0 \tag{7}$$

which is the familiar Newton–Euler angular momentum relationship. If we expand Eq. (7) in terms of its components, we get a form of Euler's equations of rotational motion

$$h_1 = \omega_3 h_2 - \omega_2 h_3, \qquad h_2 = \omega_1 h_3 - \omega_3 h_1, \qquad h_3 = \omega_2 h_1 - \omega_1 h_2 \tag{8}$$

We eliminate the angular velocity components by computing $\boldsymbol{h} = \{\partial\mathcal{L}/\partial\boldsymbol{\omega}\}$ to get angular momentum components in terms of angular velocity components. With some simplification, we have the following equations relating the body angular momentum components h_i to the body angular velocity components ω_i, the appendage angle of twist α, and the relative rotor speed ω_r:

$$h_1 = \frac{\partial\mathcal{L}}{\partial\omega_1} = A_a\dot{\alpha} + (A_a + A_b)\omega_1 \tag{9}$$

$$h_2 = \frac{\partial\mathcal{L}}{\partial\omega_2} = \frac{1}{2}\Big[\big(2B_b + 2\Delta + B_a + C_a + 2m_ad^2\big)$$
$$+ (B_a - C_a)\cos 2\alpha\Big]\omega_2 + \frac{1}{2}\omega_3(B_a - C_a)\sin 2\alpha + I_r\omega_r \tag{10}$$

$$h_3 = \frac{\partial\mathcal{L}}{\partial\omega_3} = \frac{1}{2}\Big[\big(2C_b + 2\Delta + B_a + C_a + 2m_ad^2\big)$$
$$- (B_a - C_a)\cos 2\alpha\Big]\omega_3 + \frac{1}{2}\omega_2(B_a - C_a)\sin 2\alpha \tag{11}$$

We invert Eqs. (9–11) to solve for the angular velocity components in terms of the angular momentum components to obtain

$$\omega_1 = \frac{h_1 - A_a\dot{\alpha}}{A_a + A_b} \tag{12}$$

$$\omega_2 = (1/\mathbb{D})\Big\{\big(2C_b + 2\Delta + B_a + C_a + 2m_ad^2\big)(h_2 - I_r\omega_r)$$
$$- (B_a - C_a)[(h_2 - I_r\omega_r)\cos 2\alpha + h_3\sin 2\alpha]\Big\} \tag{13}$$

$$\omega_3 = (1/\mathbb{D})\Big\{\big(2B_b + 2\Delta + B_a + C_a + 2m_ad^2\big)h_3$$
$$+ (B_a - C_a)[h_3\cos 2\alpha - (h_2 - I_r\omega_r)\sin 2\alpha]\Big\} \tag{14}$$

where the denominator $\mathbb{D}$ in Eqs. (13) and (14) is defined to be

$$\mathbb{D} \triangleq 2\big(B_b + C_b + \Delta + B_a + C_a + m_ad^2\big)\big(\Delta + m_ad^2\big)$$
$$+ 2(B_bC_b + B_aC_a) + (B_b + C_b)(B_a + C_a)$$
$$- (B_b - C_b)(B_a - C_a)\cos 2\alpha \tag{15}$$

The complete equations of motion for the carrier body are given when we substitute Eqs. (12–14) into Eq. (8),

$$h_1 = (1/\mathbb{D})\Big\{2[B_b - C_b + (B_a - C_a)\cos 2\alpha]h_2h_3$$
$$+ \big(h_3^2 - h_2^2\big)(B_a - C_a)\sin 2\alpha + I_r\omega_r\big[h_2(B_a - C_a)\sin 2\alpha$$
$$+ h_3\big(2C_b + 2\Delta + B_a + C_a + 2m_ad^2 - (B_a - C_a)\cos 2\alpha\big)\big]\Big\} \tag{16}$$

$$h_2 = \frac{h_1h_3 - A_a\dot{\alpha}h_3}{A_a + A_b} + \frac{1}{\mathbb{D}}\Big\{h_1(h_2 - I_r\omega_r)(B_a - C_a)\sin 2\alpha$$
$$- h_1h_3\big[2B_b + 2\Delta + B_a + C_a + 2m_ad^2 + (B_a - C_a)\cos 2\alpha\big]\Big\} \tag{17}$$

$$h_3 = -\frac{h_1h_2 - A_a\dot{\alpha}h_2}{A_a + A_b} - \frac{1}{\mathbb{D}}\Big\{h_1h_3(B_a - C_a)\sin 2\alpha$$
$$- h_1(h_2 - I_r\omega_r)\big[2C_b + 2\Delta + B_a + C_a + 2m_ad^2$$
$$- (B_a - C_a)\cos 2\alpha\big]\Big\} \tag{18}$$

We now turn our attention to deriving the equation of motion for the flexible appendage. Rotation of the appendage relative to the carrier body is measured by the angle α (see Fig. 1b), which is a generalized position coordinate of the system. The equation of motion for the appendage is given by the standard Lagrange's equation relationship

$$\frac{\mathrm{d}}{\mathrm{d}t}\frac{\partial\mathcal{L}}{\partial\dot{\alpha}} - \frac{\partial\mathcal{L}}{\partial\alpha} = \mathcal{Q}_a \tag{19}$$

where $\mathcal{L}$ is the system Lagrangian given by Eq. (5) and $\mathcal{Q}_a$ is the generalized force corresponding to α and is assumed to be zero. Evaluating Eq. (19), we have the equation of motion for the appendage

$$A_a(\ddot{\alpha} + \dot{\omega}_1) - B_b(\omega_3\cos\alpha - \omega_2\sin\alpha)(\omega_2\cos\alpha + \omega_3\sin\alpha)$$
$$+ C_a(\omega_3\cos\alpha - \omega_2\sin\alpha)(\omega_2\cos\alpha + \omega_3\sin\alpha) + K\alpha = 0 \tag{20}$$

We use Eqs. (12–14) to substitute for ω_1, ω_2, and ω_3 in Eq. (20), noting that we must differentiate Eq. (12) to substitute for $\dot{\omega}_1$. From this we obtain the equation of motion for the appendage in terms of body angular momenta

$$\ddot{\alpha} = -\frac{(A_a + A_b)K\alpha}{A_aA_b} - \frac{h_1}{A_b} + \frac{\mathbb{E}(A_a + A_b)(B_a - C_a)}{A_aA_b\mathbb{D}^2} \tag{21}$$

where h_1 is given by Eq. (16) and $\mathbb{E}$ is defined to be

$$\mathbb{E} \triangleq 4\big[h_3\big(\Delta + B_a + B_b + m_ad^2\big)\cos\alpha - (h_2 - I_r\omega_r)\big(\Delta + B_a$$
$$+ C_b + m_ad^2\big)\sin\alpha\big]\big[h_3\big(\Delta + C_a + B_b + m_ad^2\big)\sin\alpha$$
$$+ (h_2 - I_r\omega_r)\big(\Delta + C_a + C_b + m_ad^2\big)\cos\alpha\big] \tag{22}$$

To obtain the equation for the motion of the rotor, we let the angle ϕ represent the coordinate of the rotor spin, thus obtaining the following Lagrange's equation for the rotor:

$$\frac{\mathrm{d}}{\mathrm{d}t}\frac{\partial\mathcal{L}}{\partial\dot{\phi}} - \frac{\partial\mathcal{L}}{\partial\phi} = \mathcal{Q}_r \tag{23}$$

where $\mathcal{L}$ is given by Eq. (5), $\dot{\phi} = \omega_r$, and $\mathcal{Q}_r$ is a generalized force corresponding to ϕ. We now define the damping torque provided by the viscous fluid to be $\mathcal{Q}_r \triangleq -\gamma\omega_r$. Evaluation of Eq. (23) leaves us with the relationship

$$\dot{\omega}_r = -\dot{\omega}_2 - \gamma\omega_r/I_r \tag{24}$$

where we differentiate Eq. (13) to get $\dot{\omega}_2$. This gives us the equation of motion of the rotor to be

$$\dot{\omega}_r = \Big\{\mathbb{D}\gamma\omega_r/I_r + (B_a - C_a)[(\dot{\mathbb{D}}/\mathbb{D})\sin 2\alpha - 2\dot{\alpha}\cos 2\alpha]h_3$$
$$+ \big[2\dot{\Delta} + 2(B_a - C_a)\dot{\alpha}\sin 2\alpha - (\dot{\mathbb{D}}/\mathbb{D})\big(2C_b + 2\Delta + B_a + C_a$$
$$+ 2m_ad^2 - (B_a - C_a)\cos 2\alpha\big)\big](h_2 - I_r\omega_r) + \mathbb{D}\dot{h}_2/I_r$$
$$- \dot{h}_3(B_a - C_a)\sin 2\alpha\Big\}\Big/\big[I_r\big(2C_b + 2\Delta + B_a + C_a + 2m_ad^2$$
$$- (B_a - C_a)\cos 2\alpha\big) - \mathbb{D}\big] + \dot{h}_2/I_r \tag{25}$$

where we differentiate Eq. (15) to obtain

$$\dot{\mathbb{D}} = 2(B_b - C_b)(B_a - C_a)\dot{\alpha}\sin 2\alpha$$
$$+ 2\dot{\Delta}\big(B_b + C_b + 2\Delta + B_a + C_a + 2m_ad^2\big) \tag{26}$$

Equations (16–18), (21), and (25) govern the dynamics of the overall system.

Nondimensionalization of the Equations of Motion

The next step is to nondimensionalize Eq. (16–18), (21), and (25). To apply Melnikov's method, we will introduce a small perturbation parameter ε. To do this, we make the following assumptions concerning the relative size of spacecraft parameters:

$$A_a = \mathcal{O}(\varepsilon), \qquad C_a = \mathcal{O}(\varepsilon), \qquad \omega_r = \mathcal{O}(\sqrt{\varepsilon})$$

$$m_a d^2 = \mathcal{O}(\varepsilon), \qquad C_a - B_a = \mathcal{O}(\varepsilon^2), \qquad B_a = \mathcal{O}(\varepsilon)$$

$$\Delta = \mathcal{O}(\varepsilon), \qquad I_r = \mathcal{O}(\sqrt{\varepsilon}), \qquad m\ell^2 = \mathcal{O}(\varepsilon), \qquad K = \mathcal{O}(\varepsilon)$$

and we assume that all other quantities are $\mathcal{O}(1)$. Physically, these assumptions mean that the appendage and oscillating submasses are small relative to the carrier body, the appendage is nearly symmetric, the amplitude of oscillation of the submasses is small, the rotor is small, and the torsional stiffness of the appendage is small. The orderings are chosen in this way so that submasses, appendage, and rotor are modeled as small perturbations to the torque-free rigid-body system. With these assumptions in mind, the following nondimensional parameters are defined:

$$\varepsilon \triangleq \frac{m\ell^2}{B_b}, \qquad \tau \triangleq \frac{ht}{B_b}, \qquad \tilde{h}_i \triangleq \frac{h_i}{h}, \qquad \lambda \triangleq \frac{m_a d^2}{m\ell^2}$$

$$\tilde{K} \triangleq \frac{K B_b}{\varepsilon h^2}, \qquad r_1 \triangleq \frac{C_b}{B_b}, \qquad r_2 \triangleq \frac{A_b}{B_b}, \qquad r_4 \triangleq \frac{A_a}{B_a}$$

$$\tilde{\gamma} \triangleq \frac{\gamma}{h}, \qquad \tilde{\Delta} \triangleq \frac{\Delta}{m\ell^2}, \qquad \tilde{\delta} \triangleq \frac{(C_a - B_a) B_b}{(m_a d^2)^2}$$

$$\tilde{I}_r \triangleq \frac{I_r}{B_b \sqrt{\varepsilon}}, \qquad \tilde{\omega}_r \triangleq \frac{B_b}{h \sqrt{\varepsilon}} \omega_r, \qquad \tilde{\mathcal{G}} \triangleq \frac{B_a}{m_a d^2} \quad (27)$$

where ε is the perturbation parameter that relates the mass of the subbodies to the inertia of the carrier body, τ is nondimensional time, $\tilde{h}_i$ (for $i = 1, 2, 3$) are the nondimensional angular momentum components, h is the magnitude of the angular momentum vector, λ relates the appendage tip mass to the mass of the submasses, r_1 and r_2 are nondimensional shape parameters of the carrier body, r_4 is the nondimensional shape parameter of the appendage tip mass, $\tilde{\delta}$ describes the symmetry of the appendage tip mass, $\tilde{K}$ is the nondimensional torsional stiffness of the appendage rod, $\tilde{\Delta}$ is the nondimensional submass amplitude, $\tilde{\mathcal{G}}$ relates appendage shape to its distance from the center of mass $\mathcal{CM}$, $\tilde{I}_r$ is the nondimensional rotor inertia, $\tilde{\omega}_r$ is the nondimensional rotor angular velocity, and $\tilde{\gamma}$ is the nondimensional viscous damping coefficient. Differentiation with respect to τ will be denoted with a prime, or $dx/d\tau = x'$, and the preceding definitions imply that $d/d\tau \triangleq (B_b/h) \, d/dt$.

Applying definitions (27) to the equations of motion (16–18), (21), and (25), and to the definitions of $\mathbb{D}$ [Eq. (15)], $\mathbb{E}$ [Eq. (22)], and $\dot{\mathbb{D}}$ [Eq. (26)] gives the full nondimensional equations of motion

$$\tilde{h}_1' = (1/\tilde{\mathbb{D}})\{2(1 - r_1 - \tilde{\mathbb{P}}\cos 2\alpha)\tilde{h}_2\tilde{h}_3 - (\tilde{h}_3^2 - \tilde{h}_2^2)\tilde{\mathbb{P}}\sin 2\alpha$$

$$+ \varepsilon\tilde{I}_r\tilde{\omega}_r[(2r_1 + \tilde{\mathbb{Q}} + \tilde{\mathbb{P}}\cos 2\alpha)\tilde{h}_3 - \tilde{h}_2\tilde{\mathbb{P}}\sin 2\alpha]\} \quad (28)$$

$$\tilde{h}_2' = \frac{\tilde{h}_1\tilde{h}_3 - \varepsilon\lambda\tilde{\mathcal{G}}r_4\alpha'\tilde{h}_3}{\varepsilon\lambda\tilde{\mathcal{G}}r_4 + r_2} - \frac{1}{\tilde{\mathbb{D}}}[\tilde{h}_1(\tilde{h}_2 - \varepsilon\tilde{I}_r\tilde{\omega}_r)\tilde{\mathbb{P}}\sin 2\alpha$$

$$+ \tilde{h}_1\tilde{h}_3(2 + \tilde{\mathbb{Q}} - \tilde{\mathbb{P}}\cos 2\alpha)] \quad (29)$$

$$\tilde{h}_3' = \frac{\varepsilon\lambda\tilde{\mathcal{G}}r_4\alpha'\tilde{h}_2 - \tilde{h}_1\tilde{h}_2}{\varepsilon\lambda\tilde{\mathcal{G}}r_4 + r_2} + \frac{1}{\tilde{\mathbb{D}}}[\tilde{h}_1\tilde{h}_3\tilde{\mathbb{P}}\sin 2\alpha$$

$$+ \tilde{h}_1(\tilde{h}_2 - \varepsilon\tilde{I}_r\tilde{\omega}_r)(2r_1 + \tilde{\mathbb{Q}} + \tilde{\mathbb{P}}\cos 2\alpha)] \quad (30)$$

$$\alpha'' = -\frac{(\varepsilon\lambda\tilde{\mathcal{G}}r_4 + r_2)\tilde{K}\alpha}{\lambda\tilde{\mathcal{G}}r_4r_2} - \frac{\tilde{h}_1'}{r_2} - \frac{\tilde{\mathbb{P}}(\varepsilon\lambda\tilde{\mathcal{G}}r_4 + r_2)\tilde{\mathbb{E}}}{\varepsilon\lambda\tilde{\mathcal{G}}r_4r_2\tilde{\mathbb{D}}^2} \quad (31)$$

$$\sqrt{\varepsilon}\tilde{\omega}_r' = \{\tilde{\gamma}\tilde{\mathbb{D}}\tilde{\omega}_r/\tilde{I}_r + \tilde{\mathbb{P}}[2\alpha'\cos 2\alpha - (\tilde{\mathbb{D}}'/\tilde{\mathbb{D}})\sin 2\alpha]\tilde{h}_3$$

$$+ [2\varepsilon\tilde{\Delta}' - (\tilde{\mathbb{D}}'/\tilde{\mathbb{D}})(2r_1 + \tilde{\mathbb{Q}} + \tilde{\mathbb{P}}\cos 2\alpha) - 2\tilde{\mathbb{P}}\alpha'\sin 2\alpha]$$

$$\times(\tilde{h}_2 - \varepsilon\tilde{I}_r\tilde{\omega}_r) + \tilde{\mathbb{D}}\tilde{h}_3'\big/(\sqrt{\varepsilon}\tilde{I}_r) + \tilde{\mathbb{P}}\tilde{h}_3'\sin 2\alpha\}\big/$$

$$\Big[\tilde{\mathbb{D}} - \sqrt{\varepsilon}\tilde{I}_r(2r_1 + \tilde{\mathbb{Q}} + \tilde{\mathbb{P}}\cos 2\alpha)\Big] + \tilde{h}_2'\big/(\sqrt{\varepsilon}\tilde{I}_r) \quad (32)$$

where $\tilde{h}_1'$, $\tilde{h}_2'$, and $\tilde{h}_3'$ in Eqs. (31) and (32) are given by Eqs. (28–30); $\tilde{\mathbb{D}}$, $\tilde{\mathbb{D}}'$, and $\tilde{\mathbb{E}}$ are given by

$$\tilde{\mathbb{D}} = 2r_1 + (r_1 + 1)\tilde{\mathbb{Q}} - (r_1 - 1)\tilde{\mathbb{P}}\cos 2\alpha + \tfrac{1}{2}(\tilde{\mathbb{Q}}^2 - \tilde{\mathbb{P}}^2)$$

$$\tilde{\mathbb{D}}' = (r_1 + 1 + \tilde{\mathbb{Q}})2\varepsilon\tilde{\Delta}' + 2(r_1 - 1)\tilde{\mathbb{P}}\alpha'\sin 2\alpha$$

$$\tilde{\mathbb{E}} = [\tilde{h}_3(2 - \tilde{\mathbb{P}} + \tilde{\mathbb{Q}})\cos\alpha - (\tilde{h}_2 - \varepsilon\tilde{I}_r\tilde{\omega}_r)(2r_1 - \tilde{\mathbb{P}} + \tilde{\mathbb{Q}})\sin\alpha]$$

$$\times[\tilde{h}_3(2 + \tilde{\mathbb{P}} + \tilde{\mathbb{Q}})\sin\alpha + (\tilde{h}_2 - \varepsilon\tilde{I}_r\tilde{\omega}_r)(2r_1 + \tilde{\mathbb{P}} + \tilde{\mathbb{Q}})\cos\alpha]$$

and the terms $\tilde{\mathbb{P}}$ and $\tilde{\mathbb{Q}}$ are defined to be

$$\tilde{\mathbb{P}} \triangleq \varepsilon^2\lambda^2\tilde{\delta}, \qquad \tilde{\mathbb{Q}} \triangleq 2\varepsilon(\lambda + \lambda\tilde{\mathcal{G}} + \tilde{\Delta}) + \varepsilon^2\lambda^2\tilde{\delta}$$

Expansion of the Nondimensional Equations of Motion in Terms of ε

Application of Melnikov's method requires that our system of equations be of the form

$$x' = f(x; \theta) + \varepsilon g(x, \tau; \theta) \quad (33)$$

where f is the unperturbed system that is, in our case, identical to the torque-free rigid body, g contains the first-order perturbation terms, $x = \{\tilde{h}_1, \tilde{h}_2, \tilde{h}_3, \alpha, \alpha', \omega_r\}$, and θ is a vector of system parameters. To put the equations of motion in the given form, a Taylor expansion of Eqs. (28–32) in powers of the perturbation parameter ε is performed, and terms up to the appropriate order are kept. The expanded equations of motion are

$$\tilde{h}_1' = [(1 - r_1)/r1]\tilde{h}_2\tilde{h}_3 + \varepsilon\big[(\lambda + \lambda\tilde{\mathcal{G}} + \tilde{\Delta})(r_1^2 - 1)\tilde{h}_2\tilde{h}_3/r_1^2$$

$$+ \tilde{I}_r\tilde{\omega}_r\tilde{h}_3\big] + \mathcal{O}(\varepsilon^2) \quad (34)$$

$$\tilde{h}_2' = [(r_1 - r_2)/(r_1r_2)]\tilde{h}_1\tilde{h}_3 + \varepsilon\Big\{[(\lambda + \lambda\tilde{\mathcal{G}} + \tilde{\Delta})r_2^2$$

$$- \lambda\tilde{\mathcal{G}}r_4r_1^2]\tilde{h}_1\tilde{h}_3\big/(r_1^2r_2^2) - \lambda\tilde{\mathcal{G}}r_4\tilde{h}_3\alpha'/r_2\Big\} + \mathcal{O}(\varepsilon^2) \quad (35)$$

$$\tilde{h}_3' = [(r_2 - 1)/r_2]\tilde{h}_1\tilde{h}_2 + \varepsilon\Big\{[\lambda\tilde{\mathcal{G}}r_4 - (\lambda + \lambda\tilde{G} + \tilde{\Delta})r_2^2]\tilde{h}_1\tilde{h}_2/r_2^2$$

$$+ \lambda\tilde{\mathcal{G}}r_4\tilde{h}_2\alpha'/r_2 - \tilde{I}_r\tilde{\omega}_r\tilde{h}_1\Big\} + \mathcal{O}(\varepsilon^2) \quad (36)$$

$$\alpha'' = -[\tilde{K}/(\lambda\tilde{\mathcal{G}}r_4)]\alpha + [(r_1 - 1)/(r_1r_2)]\tilde{h}_2\tilde{h}_3 + \mathcal{O}(\varepsilon) \quad (37)$$

$$\sqrt{\varepsilon}\tilde{\omega}_r' = -[(r_1 - r_2)/(r_1r_2)]\tilde{h}_1\tilde{h}_3 - \tilde{\gamma}\tilde{\omega}_r/\tilde{I}_r$$

$$- \sqrt{\varepsilon}\{[(r_1 - r_2)/(r_1r_2)]\tilde{I}_r\tilde{h}_1\tilde{h}_3 + \tilde{\gamma}\tilde{\omega}_r\} + \mathcal{O}(\varepsilon) \quad (38)$$

In the next section we describe a procedure to reduce Eqs. (34–38) to three equations, which have a spherical unperturbed phase space, by the elimination of Eqs. (37) and (38). Because of this procedure, we do not need to retain terms that are $\mathcal{O}(\varepsilon)$ or higher in Eqs. (37) and (38).

Melnikov Analysis

Unperturbed Phase Space

To apply Melnikov's method, the unperturbed phase space must have a structure that includes heteroclinic connections between pairs of saddle points or orbits homoclinic to a single saddle point. Melnikov's method will evaluate changes in the Poincaré map of this structure when the system is perturbed.

The unperturbed phase space for the system given in Eqs. (34–38) is found by setting $\varepsilon = 0$. Doing so eliminates the dependence of Eqs. (34–36) on Eqs. (37) and (38) and allows us to solve
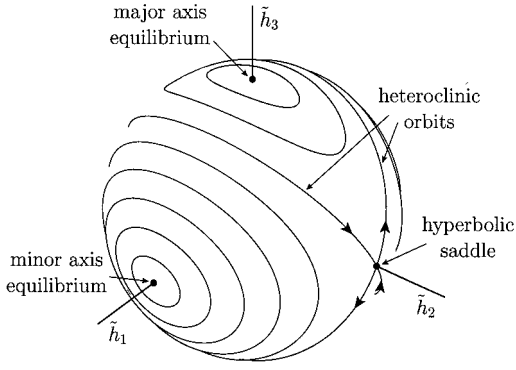
Fig. 2 Momentum sphere illustrating the heteroclinic orbits and the hyperbolic saddle points; curves are orbits of constant energy.

Eqs. (34–36) independently of Eqs. (37) and (38). The unperturbed system of equations corresponding to Eqs. (34–36) are given by

$$\tilde{h}_1' = [(1 - r_1)/r_1]\tilde{h}_2\tilde{h}_3 \tag{39}$$

$$\tilde{h}_2' = [(r_1 - r_2)/(r_1 r_2)]\tilde{h}_1\tilde{h}_3 \tag{40}$$

$$\tilde{h}_3' = [(r_2 - 1)/r_2]\tilde{h}_1\tilde{h}_2 \tag{41}$$

and are identical to Euler's rotational equations of motion for a torque-free rigid body. The phase space for the unperturbed system is a sphere shown in Fig. 2, where the nondimensional body-fixed angular momentum components, $\tilde{h}_1$, $\tilde{h}_2$, and $\tilde{h}_3$, are the phase variables. The phase space has six equilibrium points at $\{(\pm 1, 0, 0), (0, \pm 1, 0), (0, 0, \pm 1)\}$ where the equilibrium points at $(\pm 1, 0, 0)$ and $(0, 0, \pm 1)$ are neutrally stable centers corresponding to minor and major axis spin, respectively, and the equilibrium points at $(0, \pm 1, 0)$ are unstable hyperbolic saddle points corresponding to intermediate axis spin. Note the presence of heteroclinic orbits joining the pair of saddle points.

Application of Melnikov's Method

Melnikov's method is now applied to the system of Eqs. (34–38). Melnikov's method is a perturbation technique that gives global information about the system's dynamics. The method detects intersections of the stable and unstable manifolds of hyperbolic saddles in planar Poincaré maps. Existence of these intersections implies the existence of Smale horseshoes and chaos via the Smale–Birkhoff theorem (see Ref. 11). For a detailed presentation of Melnikov theory, see Guckenheimer and Holmes[11] or Wiggins.[12,13]

The most common version of Melnikov's method considers systems of the form

$$x' = f(x; \theta) + \varepsilon g(x, \tau; \theta), \qquad x = \begin{Bmatrix} u \\ v \end{Bmatrix} \in \mathbb{R}^2 \tag{42}$$

where g is periodic in τ, $f(x)$ is a Hamiltonian vector field defined on $\mathbb{R}^2$, and $\varepsilon g(x, \tau)$ is a small perturbation, which need not be Hamiltonian. It would appear that Melnikov's method would not be applicable to our system given the form of the equations in Eq. (42). That is, Melnikov's method applies to systems whose Poincaré map is planar and the system considered herein is six dimensional. On the other hand, close inspection of Eqs. (34–38) reveals that Eqs. (37) and (38) couple with Eqs. (34–36) only through the perturbation terms in Eqs. (34–36). Therefore, we can solve Eqs. (34–36) for their unperturbed solutions, that is, the solutions for $\tilde{h}_1$, $\tilde{h}_2$, and $\tilde{h}_3$ with $\varepsilon = 0$, and substitute these solutions into Eqs. (37) and (38). We then solve Eqs. (37) and (38) for their unperturbed solutions, that is, the solutions for α and $\tilde{\omega}_r$ with $\varepsilon = 0$, and then substitute the unperturbed solutions for α and $\tilde{\omega}_r$ into the perturbations of Eqs. (34–36). This process results in three nonautonomous equations in $\tilde{h}_1$, $\tilde{h}_2$, and $\tilde{h}_3$, with the unperturbed parts represented by Euler's equation of rotational motion, and perturbation terms which are function of the $\tilde{h}_i$, the system parameters, and time τ (see Refs. 44 and 45 for other examples of this procedure). This process of reducing our system to three first-order equations from six still does

not admit the application of the planar form of Melnikov's method. However, a result due to Holmes and Marsden[29] allows us to apply Melnikov's method directly to the equations involving $\tilde{h}_1$, $\tilde{h}_2$, and $\tilde{h}_3$. The Melnikov function, as given in Ref. 29, can be written

$$\mathcal{M}(\tau_0) = \int_{-\infty}^{\infty} \nabla\tilde{\mathcal{H}}[q_0(\tau)] \cdot \{f[q_0(\tau)] + g[q_0(\tau), \tau + \tau_0]\}\,d\tau \tag{43}$$

where $\nabla\tilde{\mathcal{H}}$ is the gradient of the Hamiltonian $\tilde{\mathcal{H}}$ of the unperturbed system with respect to $\tilde{h}_i$, f is the unperturbed part of the system, g is the $\mathcal{O}(\varepsilon)$ perturbation of the system, and $q_0(\tau)$ is the solution for the heteroclinic orbits or trajectories of the unperturbed system. The nondimensional Hamiltonian for the system is given by $\tilde{\mathcal{H}} = \frac{1}{2}(\tilde{h}_1^2/r_2 + \tilde{h}_2^2 + \tilde{h}_3^2/r_1)$ and is simply the kinetic energy of the unperturbed system, that is, of the carrier body. The gradient of $\tilde{\mathcal{H}}$ with respect to the body-fixed angular momentum components is, thus, the vector $\nabla\tilde{\mathcal{H}} = \{\tilde{h}_1/r_2, \tilde{h}_2, \tilde{h}_3/r_1\}$. Because it can be readily shown that $\nabla\tilde{\mathcal{H}} \cdot f = 0$, Eq. (43) simplifies to

$$\mathcal{M}(\tau_0) = \int_{-\infty}^{\infty} \nabla\tilde{\mathcal{H}}[q_0(\tau)] \cdot g[q_0(\tau), \tau + \tau_0]\,d\tau \tag{44}$$

Before the integral in Eq. (44) can be evaluated, we must find the solutions q_0 along the heteroclinic orbits of the unperturbed system given by Eqs. (39–49), find the unperturbed solution to Eq. (37) so that we may substitute for α' (α does not appear in the $\mathcal{O}(\varepsilon)$ terms in the perturbation g of the $\tilde{h}_i'$ equations) into the perturbation terms of Eqs. (34–36), and find the unperturbed solution to Eq. (38) so that we may substitute for $\tilde{\omega}_r$ into the perturbation terms of Eqs. (34–36).

The solution along the heteroclinic orbits can be found in terms of hyperbolic trigonometric functions.[1] These solutions are given as follows:

$$\tilde{h}_1 = s_1 \left[\frac{r_2(1 - r_1)}{r_2 - r_1}\right]^{\frac{1}{2}} \text{sech}(\mathbb{C}_1\tau) \tag{45}$$

$$\tilde{h}_2 = s_2 \tanh(\mathbb{C}_1\tau) \tag{46}$$

$$\tilde{h}_3 = s_3 \left[\frac{r_1(r_2 - 1)}{r_2 - r_1}\right]^{\frac{1}{2}} \text{sech}(\mathbb{C}_1\tau) \tag{47}$$

where

$$\mathbb{C}_1 \triangleq \sqrt{\frac{(r_1 - 1)(1 - r_2)}{(r_1 r_2)}}$$

and $\{s_1, s_2, s_3\} = \pm 1$ such that the product $s_1 s_2 s_3 = 1$ (these permutations give all four of the heteroclinic orbits shown in Fig. 2).

We can solve Eq. (37), with $\varepsilon = 0$, for α by substituting in the unperturbed solutions for $\tilde{h}_2$ and $\tilde{h}_3$. The approximate solution to this equation is derived by Gray et al.[38] to be $\alpha = \mathcal{A}\sin(\vartheta\tau + \Phi)$, where the square of the amplitude $\mathcal{A}$ is given by

$$\mathcal{A}^2 = \left[\alpha_0 - \frac{\pi\mathbb{C}_2}{2\mathbb{C}_1^2} \text{sech}\left(\frac{\pi\vartheta}{2\mathbb{C}_1}\right)\right]^2 + \left\{\frac{\alpha_0'}{\vartheta} + \frac{\mathbb{C}_2}{9\mathbb{C}_1} + \frac{\mathbb{C}_2}{2\mathbb{C}_1^2}\right.$$
$$\times \left.\left[\pi\tanh\left(\frac{\pi\vartheta}{2\mathbb{C}_1}\right) + i\psi\left(\frac{\mathbb{C}_1 + i\vartheta}{4\mathbb{C}_1}\right) - i\psi\left(\frac{\mathbb{C}_1 - i\vartheta}{4\mathbb{C}_1}\right)\right]\right\}^2$$

the tangent of the phase angle Φ is given by

$$\tan\Phi = \left[\alpha_0 - \frac{\pi\mathbb{C}_2}{2\mathbb{C}_1^2} \text{sech}\left(\frac{\pi\vartheta}{2\mathbb{C}_1}\right)\right] \Big/ \left\{\frac{\alpha_0'}{\vartheta} + \frac{\mathbb{C}_2}{9\mathbb{C}_1}\right.$$
$$+ \left.\frac{\mathbb{C}_2}{2\mathbb{C}_1^2}\left[\pi\tanh\left(\frac{\pi\vartheta}{2\mathbb{C}_1}\right) + i\psi\left(\frac{\mathbb{C}_1 + i\vartheta}{4\mathbb{C}_1}\right) - i\psi\left(\frac{\mathbb{C}_1 - i\vartheta}{4\mathbb{C}_1}\right)\right]\right\}$$

where α_0 is the initial angle of twist of the torsional appendage, α_0' is the initial twist rate, $\psi = \psi(z)$ is Euler's digamma function defined for complex variables, ϑ is the frequency of appendage oscillation defined by $\vartheta \triangleq \sqrt{[\tilde{K}/(\lambda\tilde{\mathcal{G}}r_4)]}$, and $\mathbb{C}_2$ is defined by

$$\mathbb{C}_2 \triangleq \frac{r_1 - 1}{r_1 r_2}\sqrt{\frac{r_1(1 - r_2)}{r_1 - r_2}}$$

When we let $\varepsilon = 0$ in Eq. (38), we get an algebraic equation, which we solve directly for $\tilde{\omega}_r$ as

$$\tilde{\omega}_r = -(\tilde{I}_r/\tilde{\gamma})[(r_1 - r_2)/(r_1 r_2)]\tilde{h}_1 \tilde{h}_3 \qquad (48)$$

where $\tilde{h}_1$ and $\tilde{h}_3$ are given by Eqs. (45) and (47), respectively.

We will now prescribe the motion of the displacement function of the submasses $\eta(t)$ to be harmonic. In dimensional terms, we let the displacement function be $\eta(t) = \eta_0 \cos(\Omega t)$, where η_0 is the maximum amplitude of displacement and Ω is the frequency of oscillation. We nondimensionalize this definition of the displacement function by letting $\tilde{\Omega} = \Omega B_b / h = \Omega t / \tau$ and $\tilde{\eta}_0 = \eta_0 / \ell$ so that the prescribed displacement becomes $\tilde{\eta}(\tau) = \tilde{\eta}_0 \cos(\tilde{\Omega}\tau)$ and the definition of $\tilde{\Delta}$ becomes

$$\tilde{\Delta}(\tau) = \tilde{\eta}_0^2 + 4\tilde{\eta}_0 \cos(\tilde{\Omega}\tau) + \tilde{\eta}_0^2 \cos(2\tilde{\Omega}\tau) \qquad (49)$$

In accordance with Melnikov's method, we now replace τ by $\tau + \tau_0$ everywhere that τ appears explicitly. There are two explicit appearances of time in our model: one is in the solution for $\alpha' = \mathcal{A}\vartheta \cos(\vartheta\tau + \Phi)$ and the other is in the displacement function of the submasses $\tilde{\eta}(\tau)$, which enters the perturbation terms through $\tilde{\Delta}$. Noting this, and then replacing τ by $\tau + \tau_0$ in both $\tilde{\Delta}$ and α', we then substitute the resulting expression for $\tilde{\Delta}$ and α' into Eqs. (34–36) to obtain the final form of the Melnikov integral.

Melnikov Function

The Melnikov integral given in Eq. (44) is now expanded, and the unperturbed solutions (45–47), along the heteroclinic orbits, are substituted for $\tilde{h}_1$, $\tilde{h}_2$, and $\tilde{h}_3$ in the integral. Because the integral is performed over the interval $(-\infty, \infty)$, all odd functions in the integrand can be eliminated leaving the following terms in the Melnikov integral:

$$\mathcal{M}(\tau_0) = \mathcal{A}\vartheta\lambda\tilde{\mathcal{G}}r_4\mathbb{C}_2 \int_{-\infty}^{\infty} \mathrm{sech}(\mathbb{C}_1\tau)\tanh(\mathbb{C}_1\tau)\sin(\vartheta\tau)$$

$$\times \sin(\vartheta\tau_0 + \Phi)\,\mathrm{d}\tau - 4\tilde{\eta}_0\mathbb{C}_1\mathbb{C}_3 \int_{-\infty}^{\infty}\mathrm{sech}^2(\mathbb{C}_1\tau)\tanh(\mathbb{C}_1\tau)$$

$$\times \sin(\tilde{\Omega}\tau)\sin(\tilde{\Omega}\tau_0)\,\mathrm{d}\tau - \tilde{\eta}_0^2\mathbb{C}_1\mathbb{C}_3 \int_{-\infty}^{\infty}\mathrm{sech}^2(\mathbb{C}_1\tau)\tanh(\mathbb{C}_1\tau)$$

$$\times \sin(2\tilde{\Omega}\tau)\sin(2\tilde{\Omega}\tau_0)\,\mathrm{d}\tau - \frac{\mathbb{C}_1^2\tilde{I}_r^2}{\tilde{\gamma}} \int_{-\infty}^{\infty}\mathrm{sech}^4(\mathbb{C}_1\tau)\,\mathrm{d}\tau \qquad (50)$$

where $\mathbb{C}_3$ is defined by

$$\mathbb{C}_3 \overset{\Delta}{=} \frac{(r_1 - 1)(r_1 - r_2 + 1)}{r_1(r_1 - r_2)}.$$

The integrals in Eq. (50) can be evaluated symbolically with Mathematica 4 (Ref. 46). After integrating, we arrive at the Melnikov function for our system of equations:

$$\mathcal{M}(\tau_0) = \frac{\mathcal{A}\vartheta^2\lambda\tilde{\mathcal{G}}r_4\mathbb{C}_2}{\mathbb{C}_1^2}\,\mathrm{sech}\left(\frac{\pi\vartheta}{2\mathbb{C}_1}\right)\sin(\Phi + \vartheta\tau_0)$$

$$- \frac{4\mathbb{C}_1\tilde{I}_r^2}{3\tilde{\gamma}} - \frac{2\pi\tilde{\eta}_0\tilde{\Omega}^2\mathbb{C}_3}{\mathbb{C}_1^2}\left[\mathrm{csch}\left(\frac{\pi\tilde{\Omega}}{2\mathbb{C}_1}\right)\sin(\tilde{\Omega}\tau_0)\right.$$

$$\left. + \tilde{\eta}_0\,\mathrm{csch}\left(\frac{\pi\tilde{\Omega}}{\mathbb{C}_1}\right)\sin(2\tilde{\Omega}\tau_0)\right] \qquad (51)$$

Because the Melnikov function is a measure of distance between stable and unstable manifolds in the Poincaré map of our system, zeros of the Melnikov function indicate intersections of the two manifolds. The function contains four terms, one of which is constant and the other three vary sinusoidally with τ_0. Zeros of this function will occur whenever the combined amplitude of the three

sinusoidal terms is greater than the constant term. Deriving the maximum combined amplitude of the two terms whose frequencies are multiples of $\tilde{\Omega}$ to be

$$F_{\max} = \left(\frac{3\mathbb{A}}{4} + \frac{\sqrt{\mathbb{A}^2 + 32\mathbb{B}^2}}{4}\right)\sqrt{\frac{1}{2} - \frac{\mathbb{A}^2}{32\mathbb{B}^2} + \frac{\mathbb{A}\sqrt{\mathbb{A}^2 + 32\mathbb{B}^2}}{32\mathbb{B}^2}}$$

where we define $\mathbb{A}$ and $\mathbb{B}$ to be

$$\mathbb{A} \overset{\Delta}{=} \mathrm{csch}[\pi\tilde{\Omega}/(2\mathbb{C}_1)], \qquad \mathbb{B} \overset{\Delta}{=} \tilde{\eta}_0\,\mathrm{csch}(\pi\tilde{\Omega}/\mathbb{C}_1)$$

the Melnikov criterion becomes

$$\left|\frac{\pi\mathcal{A}\vartheta^2\lambda\tilde{\mathcal{G}}r_4\mathbb{C}_2}{\mathbb{C}_1^2}\right|\left|\mathrm{sech}\left(\frac{\pi\vartheta}{2\mathbb{C}_1}\right)\right| + \left|\frac{2\pi\tilde{\eta}_0\tilde{\Omega}^2\mathbb{C}_3}{\mathbb{C}_1^2}\right|F_{\max} > \left|\frac{4\mathbb{C}_1\tilde{I}_r^2}{3\tilde{\gamma}}\right| \qquad (52)$$

This criterion is valid provided that the perturbation parameter ε is sufficiently small.

Comparison of the Melnikov Result with Numerical Simulations

We have analytically derived a criterion that predicts the existence of horseshoes in the attitude motion of a satellite perturbed by continuous elastic elements, oscillating submasses, and an energy dissipating rotor in a viscous fluid. The derived criterion can be used to find the hypersurface separating the regions of parameter space predicted to be chaotic from those predicted to be nonchaotic according to the Melnikov criterion. Inspection of Eq. (52) reveals that the Melnikov criteria are a function of 10 of the 12 nondimensional system parameters (r_1, r_2, r_4, λ, $\tilde{K}$, $\tilde{\Omega}$, $\tilde{\eta}_0$, $\tilde{\mathcal{G}}$, $\tilde{I}_r$, and $\tilde{\gamma}$). The numerical simulations include the other two system parameters, ε and $\tilde{\delta}$, although they do not appear in the Melnikov criterion because ε generally does not appear in Melnikov criterion and because we assumed that $\tilde{\delta}$ was $\mathcal{O}(\varepsilon^2)$. If we satisfy Eq. (52) and the aforementioned restriction on the carrier body's shape parameters r_1 and r_2 (where $0 < r_2 < 1 < r_1 < 1 + r_2$), then the system, modeled by Eqs. (28–31), exhibits chaotic dynamics near the unperturbed heteroclinic orbits for sufficiently small ε.

Investigation of those regions of parameter space predicted to be chaotic according to the Melnikov criterion given in Eq. (52) can be performed by fixing 7 of the 10 system parameters and then studying the surface generated by the others in a three-dimensional parameter subspace. Unfortunately, this reveals little more than a general qualitative picture of the Melnikov prediction. In addition, it does nothing to tell us how good the Melnikov criterion is in predicting the actual behavior of the system. On the other hand, numerical simulation in concert with the Melnikov criterion can tell us not only when the Melnikov criterion is applicable and when it is not, but also can tell us the types of behavior exhibited by this system as well as those values of the system parameters for which each type of behavior occurs.

Classes of Dynamical Behavior and Their Automatic Determination

We begin by showing the three major classes of behavior exhibited by this system. Each of the different classes of behavior can be realized by simply altering appropriate combinations of the 12 system parameters. What is of interest, of course, are those values of the system parameters that give each type of behavior. The trajectories shown in Figs. 3 and 4 show the types of behavior we observed, and were generated using the double precision lsode routine from ODEPACK.[47] Each trajectory is shown on the surface of the momentum sphere in $\tilde{h}_1$-$\tilde{h}_2$-$\tilde{h}_3$ space, and the two great circles passing through the $\tilde{h}_2$ axis are the unperturbed heteroclinic cycles. In all simulations discussed herein, the absolute and relative tolerances were set to 10^{-7}, and the initial conditions were $\tilde{h}_1 = \cos(5 \deg)$, $\tilde{h}_2 = \sin(5 \deg)$, $\tilde{h}_3 = 0$, $\alpha = 0$, $\alpha' = 0$, and $\tilde{\omega}_r = 0.5$.

Figure 3a shows a trajectory typical of those that decay to major axis spin (MAS). Note that even though we designate these trajectories as decaying to MAS, because the system is being forced periodically, these trajectories are, in fact, very small limit cycles, that is, they have a radius of less than 0.02 on the unit sphere. The values of the system parameters used to generate Fig 3a, as well as

those used to generate all other trajectories in Figs. 3 and 4, may be found in Table 1.

Figure 3b shows a trajectory typical of those that eventually end up in a period-1 limit cycle about major axis spin. The dark, wide band around the $\tilde{h}_3$ axis at the top of the momentum sphere is the limit cycle.

Figure 3c shows a trajectory typical of those that are chaotic. It is readily seen that the trajectory does not settle down into a regular pattern, decaying to neither MAS nor a limit cycle. In fact, chaotic trajectories eventually fill all of the momentum sphere except for small regions surrounding minor axis spin that is, $\pm \tilde{h}_1$ axis.

The trajectories shown in Fig. 4 represent three of a myriad of other types of trajectories that have been numerically discovered in this system. They are the minority of the trajectories that have been encountered, representing less than 5–10% of all trajectories. On the other hand, note that they probably represent bifurcations on the way to chaotic trajectories. The transient part of the trajectory is not shown, to better highlight the steady-state structure of the orbits. Figure 4a is an interesting period-3 limit cycle in which the trajectory alternately changes direction as it goes around each

of the three loops in the trajectory. Figure 4b is the tail end of a quasi-periodic trajectory. Figure 4c is a period-1 limit cycle of a completely different nature and physically represents a spacecraft that alternately spins about its positive and negative major axes.

Now that we have seen the types of behavior that can occur in this system, it is of interest to locate those regions of parameter space in which each major class of behavior occurs. After doing so, it is then easy to compare these numerically generated results with the predictions of the Melnikov criterion. Figures 5–9 show the $\tilde{\Omega}$ vs $\tilde{\eta}_0$ region of the parameter space for a number of different values of the other parameters. Because of the high dimension of the parameter space, it is prohibitive to study all combinations of two-dimensional parameter spaces in detail, so we have chosen some of the parameters we feel are of fundamental importance to the system. In each of Figs. 5–9, the Melnikov result is superimposed on each subplot and is the dark U-shaped curve that is concave to the right. In each case, large black dots are chaotic trajectories, open circles are limit-cycle trajectories, and the small dots are trajectories that damp to MAS.

To determine the class of behavior for each parameter value, the system is integrated for a period of time sufficiently long enough so that all transients will have decayed. We then take advantage of the unique structure of each of the trajectory types on the momentum sphere in the following manner:

1) Trajectories that end up in MAS (Fig. 3a) do not have a large variation in $\tilde{h}_1$, $\tilde{h}_2$, or $\tilde{h}_3$ after the initial transient part of the trajectory is removed [we use 2^{16} time steps, each of which is 0.2 nondimensional time units, and then use the last 2% of the trajectory]. By the use of this knowledge, if the standard deviation of $\tilde{h}_1$ and $\tilde{h}_2$ is less than 0.015, then the trajectory is deemed to be one which ends in MAS.

2) Trajectories ending in period-n limit cycles about the major axis (see Fig. 3b) generally have a small variation in $\tilde{h}_3$ and a much larger variation in $\tilde{h}_1$ and $\tilde{h}_2$. Additionally, we have observed that some trajectories end up in limit cycles about the minor axis. Therefore, if the trajectory has not been deemed to end in MAS and the standard deviation of $\tilde{h}_1$ or $\tilde{h}_3$ is less than 0.175, then the trajectory is designated as ending in a period-n limit cycle.

Table 1 Parameters used in Figs. 3 and 4 to generate trajectories

| Parameter	MAS, Fig. 3a	Period-1, Fig. 3b	Chaotic, Fig. 3c	Period-3, Fig. 4a	Quasi periodic, Fig. 4b	Baseball, Fig. 4c
ε	0.20	0.20	0.20	0.20	0.20	0.20
$\tilde{\Omega}$	0.15	1.40	0.90	0.35	1.95	0.55
$\tilde{\eta}_0$	0.20	1.15	1.30	1.30	0.55	1.55
$\tilde{\gamma}$	5.00	5.00	5.00	5.00	5.00	5.00
I_r	1.00	1.00	1.00	1.00	1.00	1.00
r_1	1.50	1.50	1.50	1.10	1.50	1.50
r_2	0.60	0.60	0.60	0.90	0.60	0.60
r_4	1.00	1.00	1.00	1.00	1.00	1.00
K	2.50	2.50	2.50	2.50	2.50	2.50
λ	0.10	0.10	0.10	0.10	1.10	0.10
$\tilde{\mathcal{G}}$	0.10	0.10	0.10	0.10	1.10	0.10
δ	0.00	0.00	0.00	0.00	0.00	0.00
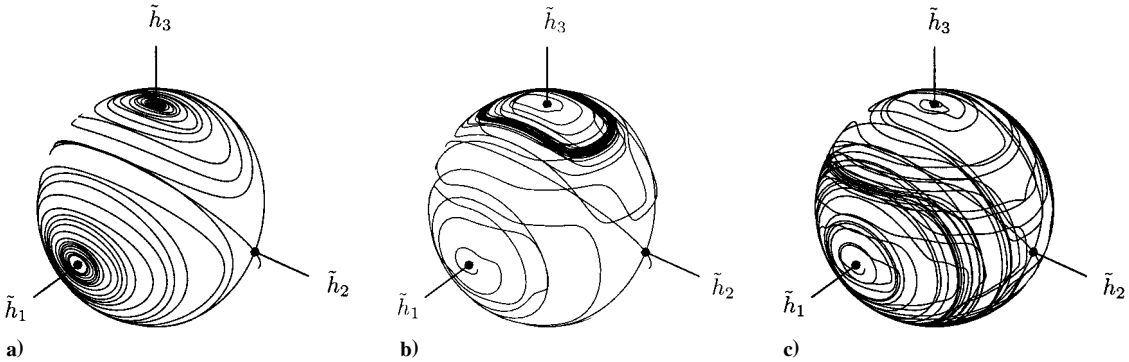
Fig. 3   Examples of trajectories depicting the three major classes of observed behavior.
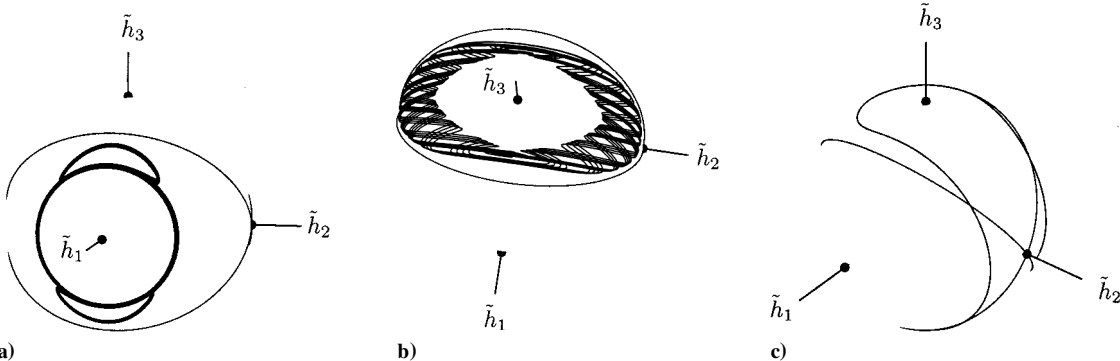

Fig. 4   Examples of trajectories depicting three interesting and unusual classes of observed behavior.
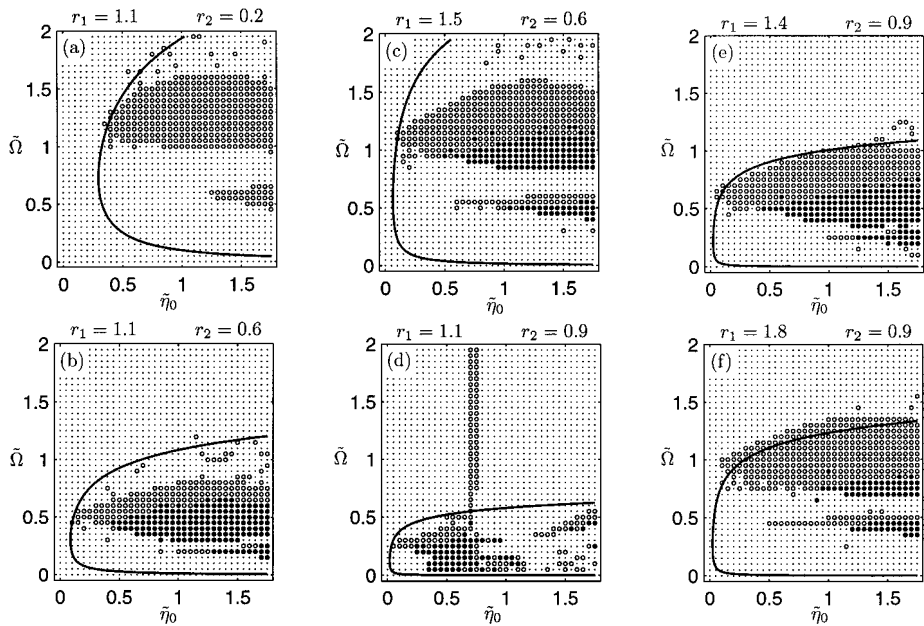
Fig. 5   Evolution of $\tilde{\eta}_0$–$\tilde{\Omega}$–r_2–r_1 parameter space with $\varepsilon = 0.2$, $r_4 = 1.0$, $\tilde{K} = 2.5$, $\lambda = 0.1$, $\tilde{\mathcal{G}} = 0.1$, $\tilde{\delta} = 0.0$, $\tilde{\gamma} = 5.0$, and $\tilde{I}_r = 1.0$.
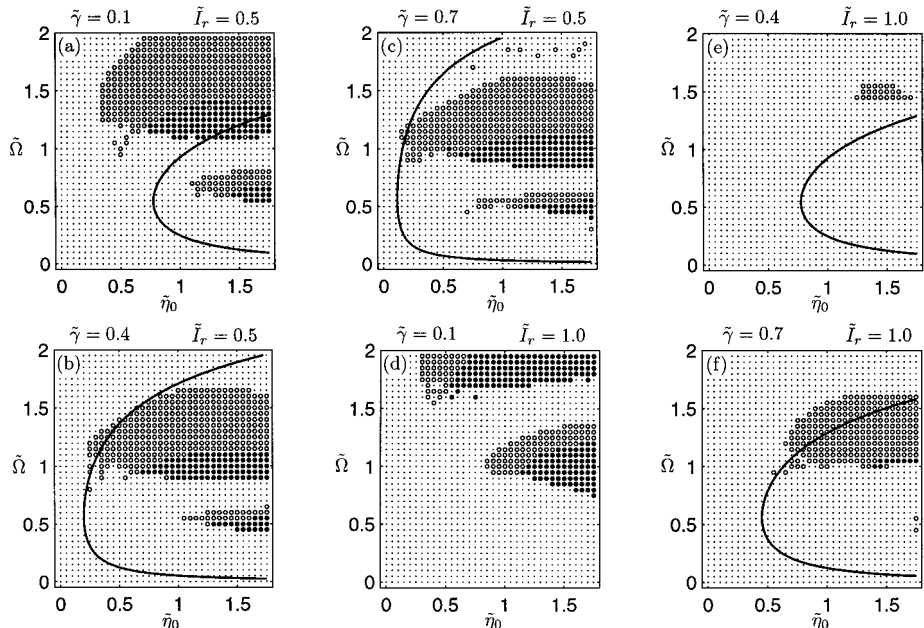

Fig. 6   Evolution of $\tilde{\eta}_0$–$\tilde{\Omega}$–$\tilde{\gamma}$–$\tilde{I}_r$ parameter space with $\varepsilon = 0.2$, $r_4 = 1.0$, $\tilde{K} = 2.5$, $\lambda = 0.1$, $\tilde{\mathcal{G}} = 0.1$, $\tilde{\delta} = 0.0$, $r_1 = 1.5$, and $r_2 = 0.6$.

3) Generally, unlike trajectories which end in either MAS or period-n limit cycles, chaotic trajectories fill a large part of the momentum sphere. Consequently, we have found that chaotic trajectories do not satisfy either of the preceding two conditions.

The enumerated procedure for determining behavior type has a significant time advantage over using measures such as Lyapunov exponents[48]; on the other hand, it is not without its disadvantages. For example, the trajectory shown in Fig. 4a is properly designated by our criteria as a period-n limit cycle. On the other hand, the trajectory shown in Fig. 4b is designated as chaotic by our criterion when, in fact, it is a quasi-periodic trajectory; however, labeling a quasi-periodic trajectory as chaotic is not far from the truth. In addition, even though the trajectory in Fig. 4c is a period-1 limit cycle, our criterion labels it as being chaotic. The code used to generate parameter spaces such as those shown in Figs. 5–9 is a work in progress, and we are changing and refining it as we discover classes of behavior that are not properly captured by our criteria. We now discuss the results of the numerical simulation.

Numerical and Analytical Study of the Parameter Space

Figure 5 shows the $\tilde{\Omega}$ vs $\tilde{\eta}_0$ region for different values of r_1 and r_2, representing different shapes of the carrier body. The eight other parameters remain fixed for these simulations. It can be seen that the interesting behavior, that is, period-n limit cycles and chaotic dynamics, occurs almost exclusively in the Melnikov region in Figs. 5a–5c and the chaotic behavior lies within the Melnikov region in all six parameter spaces shown in Fig. 5. The values of r_1 and r_2 used in Fig. 5a correspond to a prolate, that is, long and thin, carrier body, whereas the values of r_1 and r_2 used in Figs. 5c, 5e, and 5f correspond to carrier bodies that are oblate, for example, a coin. Figure 5b is also prolate like Fig. 5a, but is less so, and Fig. 5d is nearly a cube in that all three principal mass moments of inertia are nearly equal. Melnikov's method has excellent agreement with the numerical results, bounding both chaotic and limit-cycle behavior in all cases except Fig. 5d. Figure 5d is the first parameter space we have observed exhibiting this unusual behavior. In general, the MAS points on the left side of the vertical line of periodic points occurring at $\tilde{\eta}_0 \approx 0.75$ are truly MAS points. The points labeled MAS on the
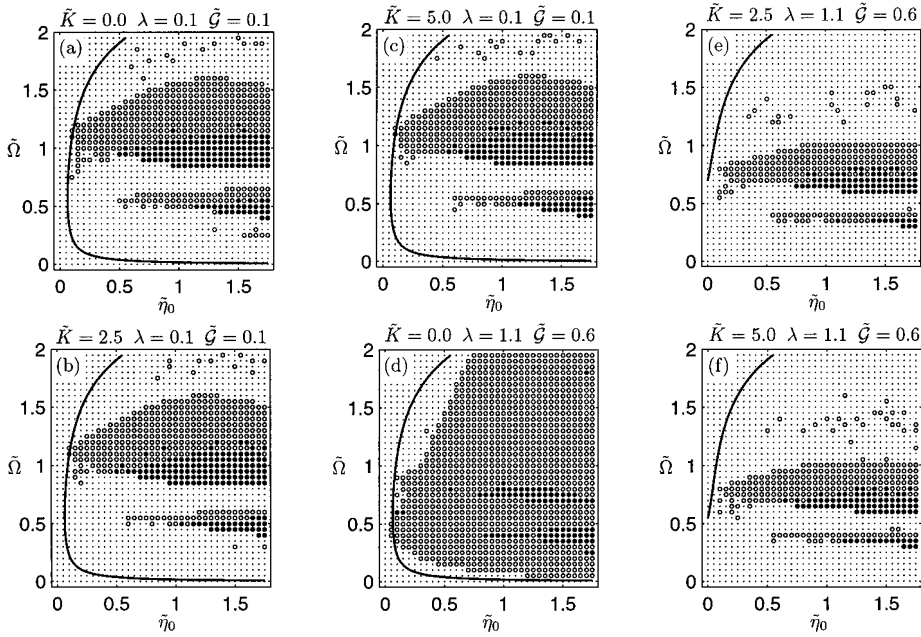
Fig. 7 Evolution of $\tilde{\eta}_0$-$\tilde{\Omega}$-$\tilde{K}$-λ-$\tilde{\mathcal{G}}$ parameter space with $\varepsilon = 0.2$, $r_1 = 1.5$, $r_2 = 0.6$, $r_4 = 1.0$, $\tilde{\delta} = 0.0$, $\tilde{\gamma} = 5.0$, and $\tilde{I}_r = 1.0$.
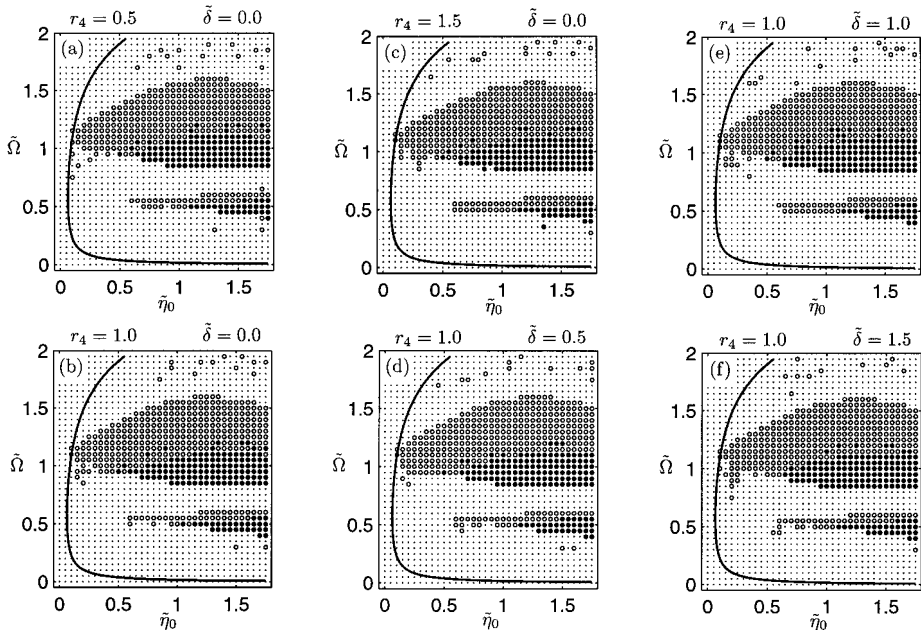
Fig. 8 Evolution of $\tilde{\eta}_0$-$\tilde{\Omega}$-r_4-$\tilde{\delta}$ parameter space with $\varepsilon = 0.2$, $r_1 = 1.5$, $r_2 = 0.6$, $\lambda = 0.1$, $\tilde{\mathcal{G}} = 0.1$, $\tilde{K} = 2.5$, $\gamma = 5.0$, and $\tilde{I}_r = 1.0$.

right side of that vertical line generally correspond to trajectories that decay to spin about the $\bar{h}_1$ axis. In fact, the trajectory in Fig. 4a corresponds to a periodic point in the lower right corner of Fig. 5d. The origin of this behavior in which trajectories decay to minor axis spin is currently under investigation.

Figure 6 shows the $\tilde{\Omega}$ vs $\tilde{\eta}_0$ region for different values of $\tilde{\gamma}$ and $\tilde{I}_r$, representing values of the coefficient of viscous damping and rotor sizes, respectively. Figures 6a–6c show increasing values of $\tilde{\gamma}$ for a relatively small rotor and Figs. 6d and 6e show the same increasing values of $\tilde{\gamma}$ for a relatively large rotor. We see that a smaller rotor displays larger regions of chaotic behavior, and this is reflected in the Melnikov curve. This makes sense physically because a larger rotor should dissipate more energy than a smaller rotor. Referring to Figs. 6d–6f and 5c, we see that for a given value of $\tilde{I}_r$, increasing $\tilde{\gamma}$ takes us from a parameter space possessing a large amount of chaos (Fig. 6d) to one possessing no chaos (Fig. 6e) and then finally to one again possessing a lot of chaos (Fig. 5c). The phenomenon

being demonstrated by this behavior is the rigidification of the rotor relative to the carrier body as the viscosity of the coupling fluid is increased. This means increasing $\tilde{\gamma}$, that is, making the fluid thicker, decreases the rate of energy dissipation and it is energy dissipation that suppresses chaos. On the other hand, the Melnikov curve is only accurate for larger values of $\tilde{\gamma}$ because we have assumed $\tilde{\gamma}$ to be $\mathcal{O}(1)$. Thus, our Melnikov result does not apply for small $\tilde{\gamma}$. Finally, we note that another consequence of the Melnikov curve not applying for small $\tilde{\gamma}$ is seen in Fig. 6d, in which $\tilde{\gamma}$ is small; note that the Melnikov curve does not appear and, hence, clearly does not enclose the chaotic behavior.

Figure 7 shows the $\tilde{\Omega}$ vs $\tilde{\eta}_0$ region for different values of $\tilde{K}$ and two different sets of values for λ and $\tilde{\mathcal{G}}$. The parameter $\tilde{K}$ is a measure of the stiffness of the torsional rod, λ is a measure of appendage size relative to the submass size, and $\tilde{\mathcal{G}}$ is a measure of the size of the appendage. Figures 7a–7c vary $\tilde{K}$ for one set of λ and $\tilde{\mathcal{G}}$ and Figs. 7d–7f vary $\tilde{K}$ for another set. Figures 7a–7c show little
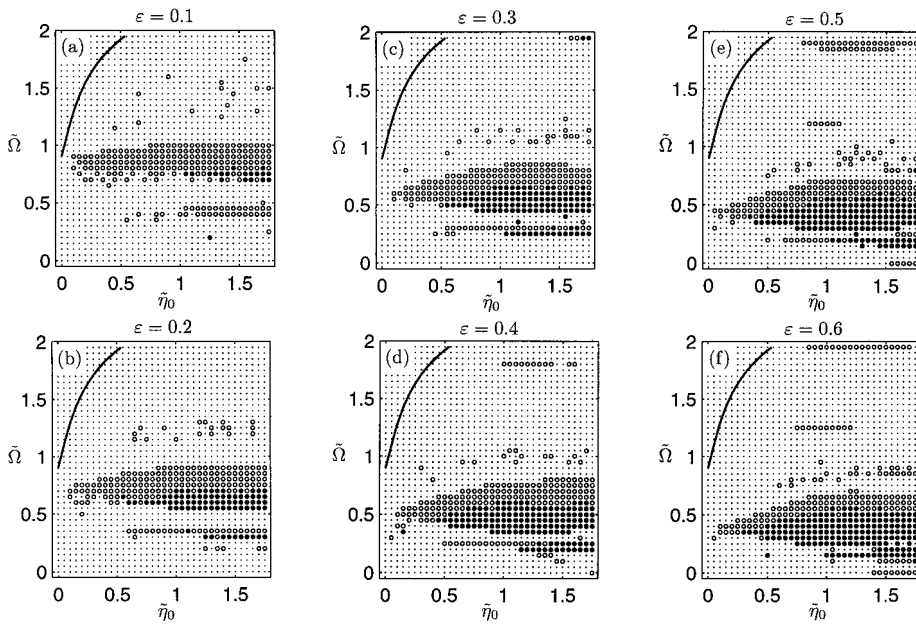
Fig. 9 Evolution of $\tilde{\eta}_0$-$\tilde{\Omega}$-ε parameter space with $r_1 = 1.5$, $r_2 = 0.6$, $r_4 = 1.0$, $\tilde{\delta} = 0.0$, $\lambda = 1.0$, $\tilde{\mathcal{G}} = 1.0$, $\tilde{K} = 2.5$, $\tilde{\gamma} = 5.0$, and $\tilde{I}_r = 1.0$.

change in either the Melnikov curve or the type of dynamics found numerically, indicating that the system is insensitive to changes in the torsional stiffness for these values of λ and $\tilde{\mathcal{G}}$. When λ and $\tilde{\mathcal{G}}$ are increased in Figs. 7d–7f, we see that changing $\tilde{K}$ now has a noticeable impact on the region of nonlinear behavior, that is, chaos and limit cycles. Because increasing λ and $\tilde{\mathcal{G}}$ is effectively making the appendage larger, it is not surprising that changing its torsional stiffness, that is, $\tilde{K}$, will now be more noticeable.

Figure 8 shows the $\tilde{\Omega}$ vs $\tilde{\eta}_0$ region for different values of r_4 and $\tilde{\delta}$. Recall that r_4 and $\tilde{\delta}$ are shape parameters for the appendage. Figures 8a–8c show three values of r_4 with $\tilde{\delta}$ held constant at zero ($\tilde{\delta} = 0$ implies that $C_a = B_a$ for the inertia terms of the appendage, that is, it is axisymmetric about the e_1–ζ_1 axis). Changing r_4 does not have a large effect on the overall dynamics, as is evidenced by both the Melnikov curve and the numerical data. Figures 8b and 8d–8f show four values of $\tilde{\delta}$ with r_4 held constant. Again, increasing $\tilde{\delta}$ does not have a large effect on the numerical data and has no effect on the Melnikov curve because $\tilde{\delta}$ does not appear in the Melnikov function.

Figure 9 shows parameter space plots for increasing values of ε, the perturbation parameter. In this case, we used $\lambda = \tilde{\mathcal{G}} = 1.0$, because numerical instabilities occurred for $\varepsilon > 0.2$ and for λ and $\tilde{\mathcal{G}}$ equal to 0.1, which were the values used in all other figures. Figures 9a–9f show ε increasing from 0.1 to 0.6. The Melnikov function is not dependent on ε, although the number of chaotic points under the Melnikov curve appears to increase as ε is increased. This is expected because higher values of ε gives the perturbation terms a larger effect on the dynamics of the spacecraft. The line of periodic trajectory points floating in the middle of Figs. 9e and 9f and near the top Figs. 9c–9f have trajectories similar to the quasi-periodic orbit shown in Fig. 4b.

The simulations shown in Figs. 5–9 are only a small, though representative, sample of the total number of simulations we performed to understand the behavior of the system being studied and the validity of Melnikov's method. As with the simulation results shown herein, our other simulations showed that Melnikov's method bounds, with few exceptions, all of the parameter space exhibiting chaotic dynamics. In addition, all of our simulations showed that even when ε is increased to large values, the Melnikov curve tends to bound those regions of parameter space exhibiting not only chaotic dynamics, but also period-n limit cycles.

Conclusions

We have derived an analytical criterion for the occurrence of a chaotic region of phase space in terms of system parameters for a

spacecraft with a nearly symmetric flexible appendage, symmetrically oscillating submasses, and a rotor immersed in a viscous fluid, a process that involves applying Melnikov's method to a perturbed satellite model and performing the calculations required to obtain a criterion for chaos that can be used in a straightforward manner for satellite design. In addition, the results of this analytical calculation are compared with extensive numerical simulations demonstrating the accuracy and utility of Melnikov's method in predicting nonlinear behavior. It is found that, with few exceptions, Melnikov's method bounds those regions of parameter space leading to chaotic dynamics. Also, it is found that, in most cases, the Melnikov criterion also bounds those regions of parameter space possessing period-n limit cycles, which is another class of potentially undesirable dynamics. The analytic criterion in this paper, thus, gives a useful design tool to spacecraft engineers concerned with avoiding potentially problematic chaotic dynamics or period-n limit cycles in their systems.

References

[1]Hughes, P. C., *Spacecraft Attitude Dynamics*, Wiley, New York, 1986, Sec. 4.3 and Chap. 7.

[2]Adams, G. J., "Dual-Spin Spacecraft Dynamics During Platform Spinup," *Journal of Guidance and Control*, Vol. 3, No. 1, 1980, pp. 29–36.

[3]Barba, P. M., and Aubrun, J. N., "Satellite Attitude Acquisition by Momentum Transfer," *AIAA Journal*, Vol. 14, No. 10, 1976, pp. 1382–1386.

[4]Cochran, J. E., and Holloway, H. E., "Resonances in the Attitude Motions of Asymmetric Dual-Spin Spacecraft," *Journal of Astronautical Sciences*, Vol. 28, No. 3, 1980, pp. 231–254.

[5]Cochran, J. E., Jr., Cheng, Y.-M., Cho, S., and Yoon, S., "Nonlinear Attitude Motion of Asymmetric Spacecraft Containing Symmetric Rotors," AIAA Paper 91-0110, Jan. 1997.

[6]Gebman, J. R., and Mingori, D. L., "Perturbation Solution for the Flat Spin Recovery of a Dual-Spin Spacecraft," *AIAA Journal*, Vol. 14, No. 7, 1976, pp. 859–867.

[7]Hall, C. D., and Rand, R. H., "Spinup Dynamics of Axial Dual-Spin Spacecraft," *Journal of Guidance, Control, and Dynamics*, Vol. 17, No. 1, 1994, pp. 30–37.

[8]Or, A. C., "Resonances in the Despin Dynamics of Dual-Spin Spacecraft," *Journal of Guidance, Control, and Dynamics*, Vol. 14, No. 2, 1991, pp. 321–329.

[9]Or, A. C., "Dynamics of an Asymmetric Gyrostat," *Journal of Guidance, Control, and Dynamics*, Vol. 21, No. 3, 1998, pp. 416–420.

[10]Or, A. C., "Chaotic Motions of a Dual-Spin Body," *Journal of Applied Mechanics*, Vol. 65, No. 1, 1998, pp. 150–156.

[11]Guckenheimer, J., and Holmes, P., *Nonlinear Oscillations, Dynamical Systems, and Bifurcations of Vector Fields*, Springer-Verlag, New York, 1983, Secs. 4.5, 5.3.

[12]Wiggins, S., *Global Bifurcations and Chaos*, Springer-Verlag, New York, 1988, Chap. 4.

[13]Wiggins, S., *Introduction to Applied Nonlinear Dynamical Systems and Chaos*, Springer-Verlag, New York, 1990, Sec. 4.5.

[14]Barba, P. M., Furumoto, N., and Leliakov, I. P., "Techniques for Flat-Spin Recovery of Spinning Satellites," AIAA Paper 73-859, 1973.

[15]Chinnery, A. E., and Hall, C. D., "Motion of a Rigid Body with an Attached Spring-Mass Damper," *Journal of Guidance, Control, and Dynamics*, Vol. 18, No. 6, 1995, pp. 1404–1409.

[16]Cronin, D. L., "Flat Spin Recovery of a Rigid Asymmetric Spacecraft," *Journal of Guidance and Control*, Vol. 1, No. 4, 1978, pp. 281, 282.

[17]Kaplan, M. H., and Cenker, R. J., "Control of Spin Ambiguity During Reorientation of an Energy Dissipating Body," *Journal of Spacecraft and Rockets*, Vol. 10, No. 12, 1973, pp. 757–760.

[18]Rahn, C. D., and Barba, P. M., "Reorientation Maneuver for Spinning Spacecraft," *Journal of Guidance, Control, and Dynamics*, Vol. 14, No. 4, 1991, pp. 724–728.

[19]Livneh, R., and Wie, B., "Asymmetric Body Spinning Motion with Energy Dissipation and Constant Body-Fixed Torques," *Journal of Guidance, Control, and Dynamics*, Vol. 22, No. 2, 1999, pp. 322–328.

[20]Tsiotras, P., and Longuski, J. M., "A Complex Analytic Solution for the Attitude Motion of a Near-Symmetric Rigid Body Under Body-Fixed Torques," *Celestial Mechanics and Dynamical Astronomy*, Vol. 51, No. 3, 1991, pp. 281–301.

[21]Longuski, J. M., and Tsiotras, P., "Analytic Solution for a Spinning Rigid Body Subject to Time-Varying Body-Fixed Torque, Part I: Constant Axial Torque," *Journal of Applied Mechanics*, Vol. 60, No. 4, 1993, pp. 970–975.

[22]Longuski, J. M., and Tsiotras, P., "Analytic Solution for a Spinning Rigid Body Subject to Time-Varying Body-Fixed Torque, Part II: Time-Varying Body-Fixed Torque," *Journal of Applied Mechanics*, Vol. 60, No. 4, 1993, pp. 976–981.

[23]Chernous'ko, F. L., "On the Motion of a Solid Body with Elastic and Dissipative Elements," *Applied Mathematics and Mechanics*, Vol. 42, No. 1, 1978, pp. 32–41.

[24]Chernous'ko, F. L., and Shamaev, A. S., "Asymptotic Behavior of Singular Perturbations in the Problem of Dynamics of a Rigid Body with Elastic and Dissipative Elements," *Mechanics of Solids*, Vol. 18, No. 3, 1983, pp. 31–41.

[25]Kaplan, M. H., and Beck, N. M., Jr., "Attitude Dynamics and Control of an Apogee Motor Assembly with Paired Satellites," *Journal of Spacecraft and Rockets*, Vol. 9, No. 6, 1972, pp. 410–415.

[26]Modi, V. J., "Attitude Dynamics of Satellites with Flexible Appendages: A Brief Review," *Journal of Spacecraft and Rockets*, Vol. 11, No. 11, 1974, pp. 743–751.

[27]Modi, V. J., "Spacecraft Attitude Dynamics: Evolution and Current Challenges," *Acta Astronautica*, Vol. 21, No. 10, 1990, pp. 689–718.

[28]Dovbysh, S. A., "Some New Dynamical Effects in the Perturbed Euler-Poinsot Problem Due to Splitting of Separatrices," *Journal of Applied Mathematics and Mechanics*, Vol. 53, No. 2, 1989, pp. 165–173.

[29]Holmes, P. J., and Marsden, J. E., "Horseshoes and Arnold Diffusion for Hamiltonian Systems on Lie Groups," *Indiana University Mathematics Journal*, Vol. 32, No. 2, 1983, pp. 273–309.

[30]Koiller, J., "A Mechanical System with a 'Wild' Horseshoe," *Journal of Mathematical Physics*, Vol. 25, No. 5, 1984, pp. 1599–1604.

[31]Tong, X., and Tabarrok, B., "Bifurcation of Self-Excited Rigid Bodies Subjected to Small Perturbation Torques," *Journal of Guidance, Control, and Dynamics*, Vol. 20, No. 1, 1997, pp. 123–128.

[32]Cooper, J. H., and Bishop, R. H., "Chaos in Rigid Body Attitude Dynamics," AIAA Paper 99-3970, Aug. 1999.

[33]Meehan, P. A., and Asokanthan, S. F., "Chaotic Motion in a Rotating Body with Internal Energy Dissipation," *Nonlinear Dynamics and Stochastic Mechanics*, edited by W. H. Kliemann, W. F. Langford, and N. S. Namachchivaya, American Mathematical Society, Providence, RI, 1996, pp. 175–202.

[34]Meehan, P. A., and Asokanthan, S. F., "Control of Chaotic Motion in a Spinning Spacecraft with a Circumferential Nutation Damper," *Nonlinear Dynamics*, Vol. 17, No. 3, 1998, pp. 269–284.

[35]Gray, G. L., Kammer, D. C., and Dobson, I., "Detection of Chaotic Saddles in an Attitude Maneuver of a Spacecraft Containing a Viscous Damper," *Advances in the Astronautical Sciences*, Vol. 82, Univelt Publishers, San Diego, CA, pp. 167–184.

[36]Gray, G. L., Kammer, D. C., Dobson, I., and Miller, A. J., "Heteroclinic Bifurcations in Rigid Bodies Containing Internally Moving Parts and a Viscous Damper," *Journal of Applied Mechanics*, Vol. 66, No. 3, 1999, pp. 720–728.

[37]Gray, G. L., Dobson, I., and Kammer, D. C., "Chaos in a Spacecraft Attitude Maneuver Due to Time-Periodic Perturbations," *Journal of Applied Mechanics*, Vol. 63, No. 2, 1996, pp. 501–508.

[38]Gray, G. L., Mazzoleni, A. P., and Campbell, D. R., III, "Analytical Criterion for Chaotic Dynamics in Flexible Satellites with Nonlinear Controller Damping," *Journal of Guidance, Control, and Dynamics*, Vol. 21, No. 4, 1998, pp. 558–565.

[39]Miller, A. J., and Gray, G. L., "Chaotic Dynamics in Flexible Satellites with Nonlinear Controller Damping and Oscillating Sub-Bodies," *Journal of the Astronautical Sciences* (submitted for publication).

[40]Mazzoleni, A. P., and Schlack, A. L., "Full Field Stability Analysis of Guy-Wired Satellites," *Journal of the Astronautical Sciences*, Vol. 43, No. 1, 1995, pp. 47–58.

[41]Mazzoleni, A. P., Hall, C. D., and Stabb, M. C., "Double Averaging Approach to the Study of Spinup Dynamics of Flexible Satellites," *Journal of Guidance, Control, and Dynamics*, Vol. 19, No. 1, 1996, pp. 54–59.

[42]Meirovitch, L., *Methods of Analytical Dynamics*, McGraw–Hill, New York, 1970, Sec. 4.12.

[43]Marsden, J. E., and Ratiu, T. S., *Introduction to Mechanics and Symmetry*, Springer-Verlag, New York, 1994, Sec. 1.2.

[44]Holmes, P., "Bifurcation and Chaos in a Simple Feedback Control System," *Proceedings of the 22nd IEEE Conference on Decision and Control*, Inst. of Electrical and Electronics Engineers, New York, 1983, pp. 365–370.

[45]Volosov, V. M., "Averaging in Systems of Ordinary Differential Equations," *Russian Mathematical Surveys*, Vol. 17, No. 6, 1962, pp. 1–126.

[46]Wolfram, S., *The Mathematica Book*, 4th ed., Cambridge Univ. Press, New York, 1999, Sec. 3.5.

[47]Hindmarsh, A. C., "ODEPACK, A Systematized Collection of ODE Solvers," *Scientific Computing*, edited by R. S. Stepleman et al., North-Holland, Amsterdam, 1983, pp. 55–64; also see http://gams.nist.gov/ to obtain the source code.

[48]Wolf, A., Swift, J. B., Swinney, H. L., and Vastano, J. A., "Determining Lyapunov Exponents from a Time Series," *Physica D*, Vol. 16, No. 3, 1985, pp. 285–317.